NRIAG JOURNAL OF ASTRONOMY AND GEOPHYSICS
2024, VOL. 13, NO. 1, 141–152
https://doi.org/10.1080/20909977.2024.2381383

Satellite land surface temperature for mapping the structurally controlled geothermal anomalies in the Cretaceous rift, South Egypt

Ahmed A. Madani and Said M. Said

Geology Department, Faculty of Science, Cairo University, Giza, Egypt

ABSTRACT

Exploration of new geothermal systems often requires regional-scale investigation. Satellite Land Surface Temperature (LST) products are essential in geothermal anomaly identification and mapping. In this study, seven thermal anomalies covering Egypt were observed using the Sentinel-3 LST images acquired in 2019 and confirmed using the 2020 LST images. In addition, the LST analysis reveals three new anomalies covering the southern part of Egypt (Kalabsha, Natash, and Wadi Allaqi), which are structurally controlled. Nuqra-Kharit-Natash is a good site for geothermal energy owing to the following reasons: 1) the high geothermal gradient beneath the Wadi Natash region (heat flow ~100 mW/m^2); 2) the presence of many geothermal anomalies retrieved from the analyses of the Landsat-8 acquired in August 2018; 3) existence of surface geothermal manifestation at the western boundary of the basin includes warm springs and the tufa deposits. Intricate structural patterns, including NW-oriented normal faults, ENE-to-WNW-oriented right-lateral faults, and NNE-oriented sinistral strike-slip faults, characterise Wadi Natash. Wadi Natash LST anomaly shows a solid relation to fault trends. High values of LST are arranged along NW and NNE faults and recorded the peak at the intersection of two fault trends. Recent seismic activity along the NNE fault system enhances the permeability along this trend and its intersection with the NW-oriented fault.

ARTICLE HISTORY
Received 4 January 2024
Revised 27 February 2024
Accepted 14 July 2024

KEYWORDS
Land surface temperature (LST); geothermal anomaly; Natash-kharit-nuqra basin; permeability of fault intersection zone; geothermal exploration

1. Introduction

Geothermal energy is a progressively essential component of renewable energy in the world. The most effective way to look for new geothermal occurrences is to first study general geographic areas based on features that suggest a favourable, cohesive geothermal system. Prospecting for geothermal anomalies can be done using a variety of geophysical techniques. However, due to in-situ geological conditions and chargeability, these technologies are typically only applicable to small-scale geothermal opportunities. The primary method for determining the land surface temperatures (LST) for regional geothermal energy exploration is satellite thermal infrared photography. Using regional structural analysis and a study of land surface temperature, this work intends to present a geothermal occurrence model. It suggests a few locations as potential geothermal hotspots where further investigation efforts should be concentrated. Future geophysical, drilling, and in-depth geological modelling exploration will be centred on this model.

The radiative skin temperature of the land that results from solar radiation (+) is known as land surface temperature (LST). The anomalous LST values were recorded when the energy stored in the Earth was added to the skin temperature. This energy represents the geothermal energy derived either from local or deep sources. Satellite LST products provide high temporal and moderate spatial resolution data that measure the LST values for large-scale areas (Zheng et al. 2019). Satellite Land Surface Temperature (LST) plays an essential role in the meteorological, hydrological, and geothermal exploration studies (Lee 1978; Coolbaugh et al. 2007; Haselwimmer et al. 2011; Jimenez-Munoz et al. 2014; van der Meer et al. 2014; Chan et al. 2018; Darge et al. 2019; Sekertekin and Arslan 2019; Madani 2020). Geothermal energy is the thermal energy stored in the Earth. It reached the Earth's surface through weak zones forming hot springs (DiPippo 2005). The rift system is the most promising tectonic setting for geothermal exploration (King and Metcalfe 2013). The East African Rift System (EARS) is an excellent example of the potential geothermal resources. It extends about 6500 Km and consists of the East African Rift (EAR), Gulf of Aden Rift, and the Red Sea Rift (Chorowicz 2005). The EAR consists of the eastern and western branches. The eastern branch possesses the essential geothermal resources in Africa. The western branch is much less active in regarding tectonics and volcanism (Darge et al. 2019).

Egypt occupies Africa's northeastern corner and includes the terminal part of the EAR (Figure 1). Generally, Egypt's northern regions have a low geothermal gradient and heat flow (Morgan and Swanberg 1978; Lashin 2007, 2015; Zaher and Ehara 2009). The Gulf of Suez and Dakhla-Kharga regions

CONTACT Said M. Said szidan@sci.cu.edu.eg Geology Department, Faculty of Science, Cairo University, Giza, Egypt

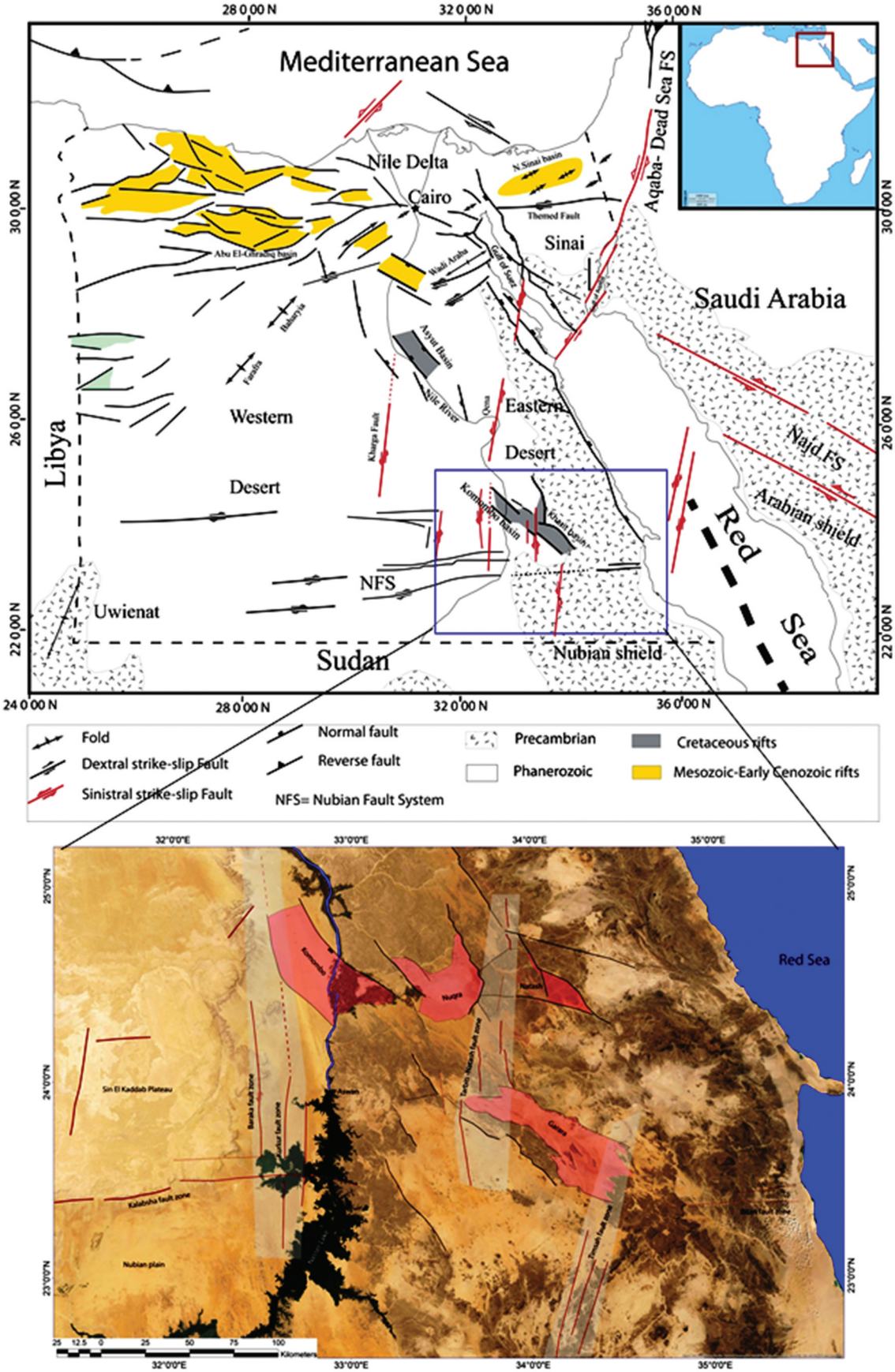

Figure 1. Location map of the study area; the upper map is the tectonic map of Egypt modified after Said and Sakran (2020), and the lower is the Bing map superimposed by the main tectonic elements in the study area.

are Egypt's most promising geothermal energy sites (Morgan *et al.*, 1985; Gad et al. 2000; El-Qady 2006; Abdel Zaher et al. 2011, 2023; Zaher et al. 2012; Elbarbary et al. 2018; Zaher and Elbarbary 2021). The heat flow beneath the Gulf of Suez's eastern coast reaches 120 mW/m^2 (Lashin and Al Arifi 2010; Lashin 2013; Abdel Zaher et al. 2014). The Dakhla and Kharga Oases are featured by many hot springs with surface temperatures up to 50°C. Several studies utilised the geochemical characteristics of the groundwater of the Dakhla-Kharga region to predict the subsurface temperatures and estimate the heat flow (Sadek 1996; Gad 2011; Tolba 2014)

The present study is the first to utilise the Sentinel-3 LST products acquired in 2019 and 2020 to reveal the anomalous LST values over the Egyptian territories and evaluate them geologically. Furthermore, evaluating the rift-related Wadi Natash volcanic field (Figure 1(B)) as a promising geothermal site and comparison to the Lake Katwe volcanic field in Uganda are additional tasks.

2. Materials and methods

An important method for investigating geothermal energy is thermal infrared remote sensing. Recent literature reviews showed that this method was used to determine the geothermal anomalies as well as the land surface temperature (LST) (Coll and Caselles 1997; Coolbaugh et al. 2007; Srivastava et al. 2009; Haselwimmer et al. 2011; Qin et al. 2011; Jimenez-Munoz et al. 2014; van der Meer et al. 2014; Sekertekin and Arslan 2019). Sentinel-3 LST products and Landsat-8 thermal band (B10) are the primary satellite data to reveal anomalous LST values over the study area. Several models were developed to retrieve the LST from satellite thermal data. All models take into consideration the atmospheric and vegetation conditions. Landsat-8 data acquired in August 2018 and covered the Kharit-Nuqra-Natash region were downloaded from the USGS website. It is prepared to retrieve the LST using a single-channel method which includes the following steps:

2.1. Calculation of sensor radiance and brightness temperature (BT)

The brightness temperature (BT) was calculated using the following two equations:

Convert the thermal DN values of band-10 into the atmosphere radiance using equation 1.

$$\lambda = \left(\frac{Lmax - Lmin}{255}\right) DN + Lmax \qquad (1)$$

L_λ is the Spectral radiance. L_{max} & L_{min} are the calibration constants extracted from the metadata file.

Convert TOA spectral radiance (L_λ) to brightness temperature (BT) using equation 2

$$CapBT = \frac{K2}{In\left(\frac{K1}{L\lambda} + 1\right)} \qquad (2)$$

BT is the Top of Atmosphere Brightness Temperature, in degree Kelvin. K_1 and K_2- thermal conversion constant. L_λ – Top of Atmospheric spectral radiance (Watts/m2 * sr * μ_m).

The ENVI v.5.3 software performs the previous equations and produces the BT image in degree Kelvin converted into a degree centigrade using the band math tool.

2.2. Derivation of Normalized Difference Vegetation Index, vegetation proportion, and land surface emissivity

This step calculates the land surface emissivity (LSE) from the Normalised Difference Vegetation Index (NDVI). Land surface emissivity measures the ability of the Earth's surface to convert heat energy into radiant energy. Several approaches were presented to calculate the land surface emissivity (LSE) from NDVI values (Sobrino and Raissouni 2000; Jimenez-Munoz et al. 2014). The Normalised Difference Vegetation Index (NDVI) is an indicator that describes the greenness, the relative density, and the health of vegetation (Sobrino and Raissouni 2000). It is derived from the visible near-infrared bands of Landsat-8 and has values ranging from (+1.0 to – 1.0). In the present study, the corrected OLI bands 4 (red) and 5 (near-infrared) were utilized to calculate the NDVI using equation 3

$$NDVI = \frac{Band5 - Band4}{Band5 + Band4} \qquad (3)$$

The previous formula's output image is used to calculate the vegetation proportion (Pv) for each pixel. The Pv image is then used to calculate land surface emissivity (LSE).

2.3. Retrieve land surface temperature (LST)

The output images of BT and LSE are used as inputs to derive LST using the following formula:

LST = ((BT)/(1+(0.00115*(BT)/1.4388) * Ln (LSE)))

The resultant LST image is sliced to reveal the anomalous LST values.

Sentinel-3 land surface temperature (LST) processing includes a split-window method; that utilized radiances from T11 & T12 channels and applies the following equation:

$LST = a_0 + b_0T_{11} + c_0T_{12}$

Where, a0, b0, and c0 are classes of coefficients that depend on atmospheric water vapor, satellite viewing

angle, and land surface emissivity. T_{11} and T_{12} represent the brightness temperatures measured at 11 μm and 12 μm, respectively. The purpose of this equation is to derive the coefficients and then the LST values.

3. Results and discussion

3.1. Mapping the geothermal anomalies using sentinel-3 LST products

Sentinel-3 is one of the European Space Agency (ESA) Sentinel satellites. It consists of two identical satellites, Sentinel-3A and Sentinel-3B. It carries multiple instruments to measure sea-surface topography, sea-land-surface temperature, ocean, and land-surface colour (https://sentinel.esa.int/web/sentinel/toolboxes/sentinel-3). Land surface temperature products are acquired using the SLSTR radiometer instrument. Level-2 data products of SLSTR are available for free. In the present study, the Sentinel-3 LST products that covered the Egyptian territories acquired in August 2019 and March 2020 are downloaded from the ESA Copernicus Hub. The pre-processing procedures include image subsets, re-projection to the UTM/WGS-84 parameters, and the LST conversion from Kelvin to Celsius. Figure 2 shows the anomalous LST values retrieved from the Sentinel-3 LST image acquired in August 2019. Inspection of the LST image revealed that: 1) No pronounced thermal anomalies are observed in Egypt's northern parts. This observation confirmed the results of previous studies, which concluded that Egypt's northern parts have low heat flow. 2). The pronounced thermal anomalies are concentrated in southern Egypt and around the Red Sea coast. 3) Seven significant geothermal anomalies are recorded (Figure 2) and confirmed using the Sentinel-3 LST images acquired in March 2020. Unfortunately, the recent image contains many clouds affecting LST values, especially in the Western Desert and the Red Sea coast. Table 1 summarises the LST values in (°C) of these 7th thermal anomalies. 4) Nuqrah- Kharit-Natash, Kalabsha, and Wadi Allaqi- Heiani regions are three new geothermal anomalies recorded for the first time during the present study. In addition, the present study evaluates the Nuqra-Kharit-Natash thermal anomaly as a potential geothermal site. 5) Many authors identify and study the Dakhla-Kharga Oases thermal anomalies (El-Sayed et al. 2006; Gad 2011), but the present study is the first that revealed their spatial dimensions.

The following section describes in detail the recorded thermal anomalies:

Kharit-Nuqra-Natash region is a new geothermal site observed using the Sentinel-3 LST product. Nuqra-Kharit basin attracts oil companies for hydrocarbon exploration. The aeromagnetic and gravity data detected the basin and described as an elongated graben bounded by rift-faults extended in the NW

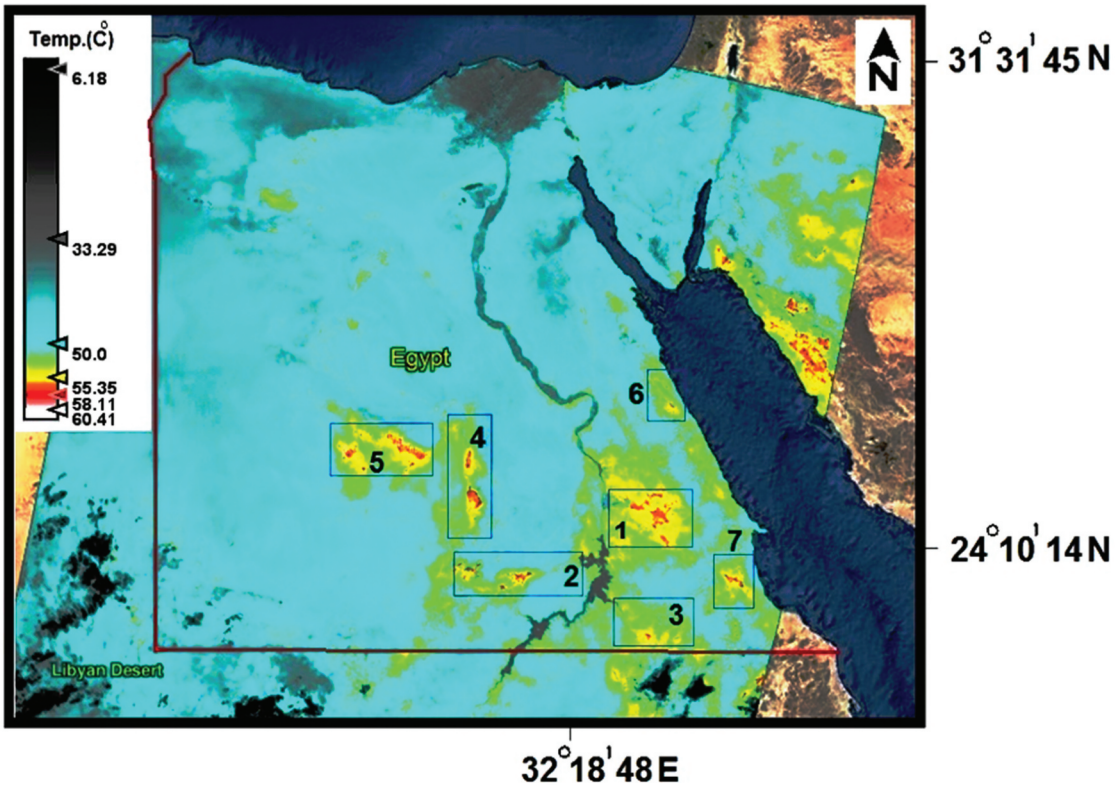

Figure 2. The 7th geothermal anomalies derived from the sentinel-3 LST product acquired in August 2019. 1: Nuqra-Kharit basin-Natash region; 2: Kalabsha area; 3: wadi allaqi-heiani belt; 4: kharga Oasis; 5: dakhla Oasis; 6: quseir region and 7: the southern extension of Nuqra- Kharit basin.

Table 1. Sentinel-3 LST values for the thermal anomalies covered Egypt.

Thermal anomalies		Sentinel-3 LST (°C), August, 2019	Sentinel-3 LST (°C), March, 2020	
Rift-related and active faults	Nuqra- Kharit- Natash and Hodein southern extension.	58	48	
		52	40	
	Kalabsha area.	59	49	
		52	42	
	Wadi Allaqi- Heiani belt.	57	49	
		52	42	
Phosphate related	Kharga Oasis.	60	Kharga-Dakhla-Quseir regions are	47
		52	covered by	42
	Dakhla Oasis.	62	Clouds	41
		52		36
	Quseir region.	58		46
		52		42

direction (Wysick 1987). Taha and Aziz (1998) considered it as the rift-basin stopped at the second/third evolutionary stage. Temperature information extracted from the wells distributed in the basin indicates the basin's moderate thermal potentiality (Kharit well records 165°F at depth 7675 ft, Kom Ombo-4 well records 143°F at 4000 ft, and Baraka-2 well records up to 157°F at a depth around 4300 ft). The basin has red/yellow colours on the LST image (Figure 2), with the anomalous LST value reaches up to 58°C recorded at the Wadi Natash volcanic region. Along the eastern shoulder of the Nuqra-Kharit basin, bimodal Natash volcanics were extruded during the Late-Jurassic and Cretaceous times (Madani 2012).

3.2. Evaluation of Kharit-Nuqra-Natash Region as a potential geothermal site

The Kharit-Nuqra-Natash region is selected as a potential geothermal site due to the following reasons: 1) many geothermal anomalies are observed in the LST image retrieved from the Landsat-8 thermal data; 2) high heat flow ~100 mW/m^2 beneath the Wadi Natash region; 3) Khariet-Nuqra-Natash is NW to NNW rift basin filled with Early to the Late Cretaceous volcano-sedimentary sequence.

3.3. Mapping the geothermal anomalies using Landsat-8 thermal data

Elaborated mapping of the Wadi Natash region's geothermal anomalies is carried out using Landsat-8 thermal data acquired in August 2018. Single-channel and split-window methods are two famous methods for LST derivation from satellite data. In the single-channel method, only one thermal band is used to retrieve the LST, whereas the split-window method utilised more than one thermal band. This study uses a single-channel method to retrieve the LST from Landsat-8 band-10 data. The method includes the following steps: 1) calculation of the sensor brightness temperature (BT) using thermal IR band-10 and derive Normalised Difference Vegetation Index (NDVI) using bands 4&5; 2) calculation of the vegetation proportion "Pv" and land surface emissivity (LSE) from the NDVI image using band math tool; 3) estimation of LST using the outputs of BT and LSE images. Figure 3 shows the LST image of the Kharit-Nuqra- Natash region. Wadi Natash volcanic region and some parts of the Nuqra-Kharit basin record anomalous LST values. The highest LST values are observed at Wadi Natash ring dykes region and scored 52°C to 54°C. Wadi Natash region has the highest LST value in the Kharit-Nuqra-Natash region.

3.3.1. Structure set up

South Egypt is characterized by complicated structure pattern which developed through long tectonic history including Pan-African event (Late Proterozoic), E-W Palaeozoic basement swell, early Cretaceous rifting, Late Cretaceous – early Tertiary Dextral transpression along E-W faults and (Sehim 1993; Moustafa et al. 2016; GEO 2018; Said and Sakran 2020, 2022; Sakran and Said 2018; Abdelhalim et al. 2023) and active sinistral shearing N-Sto NNE-SSW faults (Sakran and Said 2018). The multispectral satellite images (Landsat 8), radar images (ALOS-PALSAR), and digital elevation models (SRTM, GDEM) were used to visualize geologic structures and the primary lithology, which were validated through field survey. The resulting map shows NW NW-oriented rift system extends for about 300 km crossing the Nile valley at the Komombo area. This rift system consists of three sub-basins: Khariet, Nuqra, and Komombo (Figure 1). Four fault populations of different orientations were mapped; NW, WNW, NNE-SSE, and E-W were mapped and shown a variable amount of the dip and strike-slip components their trend relative to the main extension direction (Figure 4). NW and WNW faults are joined along their strikes developing the rift-bounded and rift interior fault systems of southern Egypt rift system.

The southern Egyptian rift system has been developed during the Early Cretaceous and consists of five NW to WNW oriented sub-basins; Gararra, Khariet, Nuqura, and Komombo and separated by NNE-SSE shear zones.

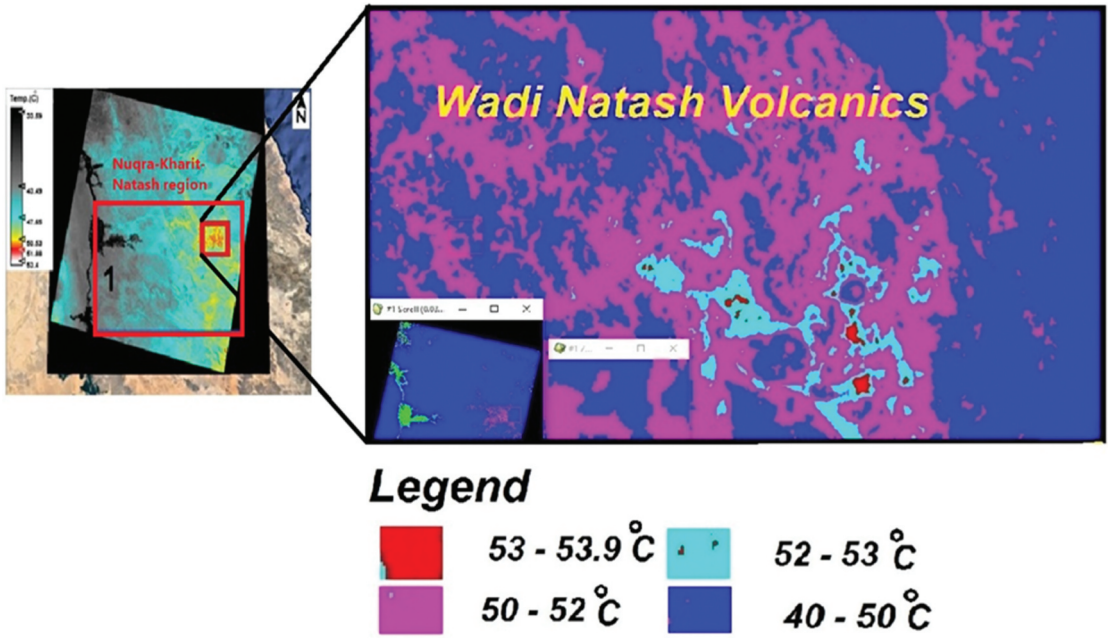

Figure 3. Landsat-8 LST image for the Nuqra-Kharit-Natash region. High-temperature regions are in cyan and red.

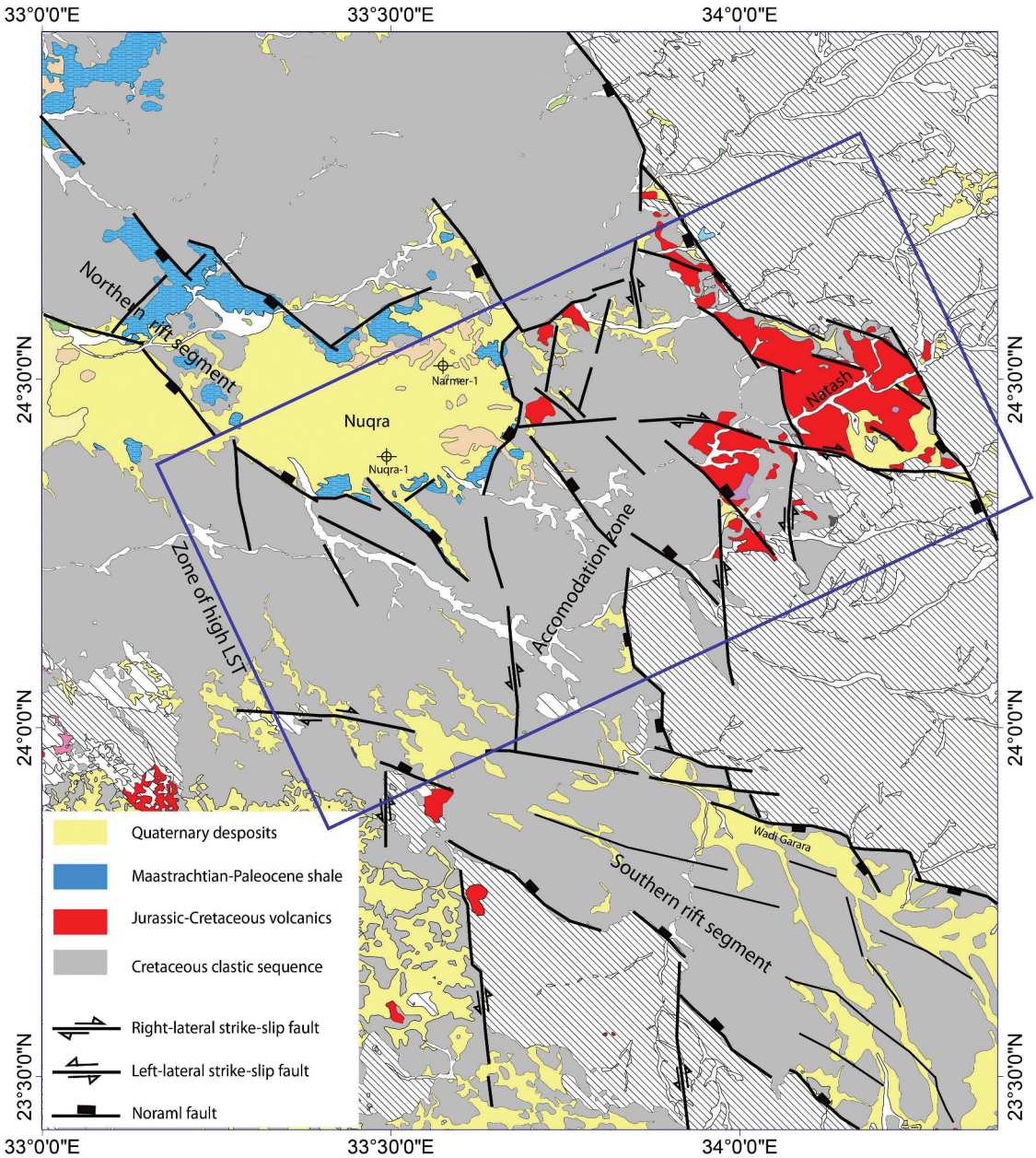

Figure 4. Geological map of the Nuqra-Natash and Garara rift system.

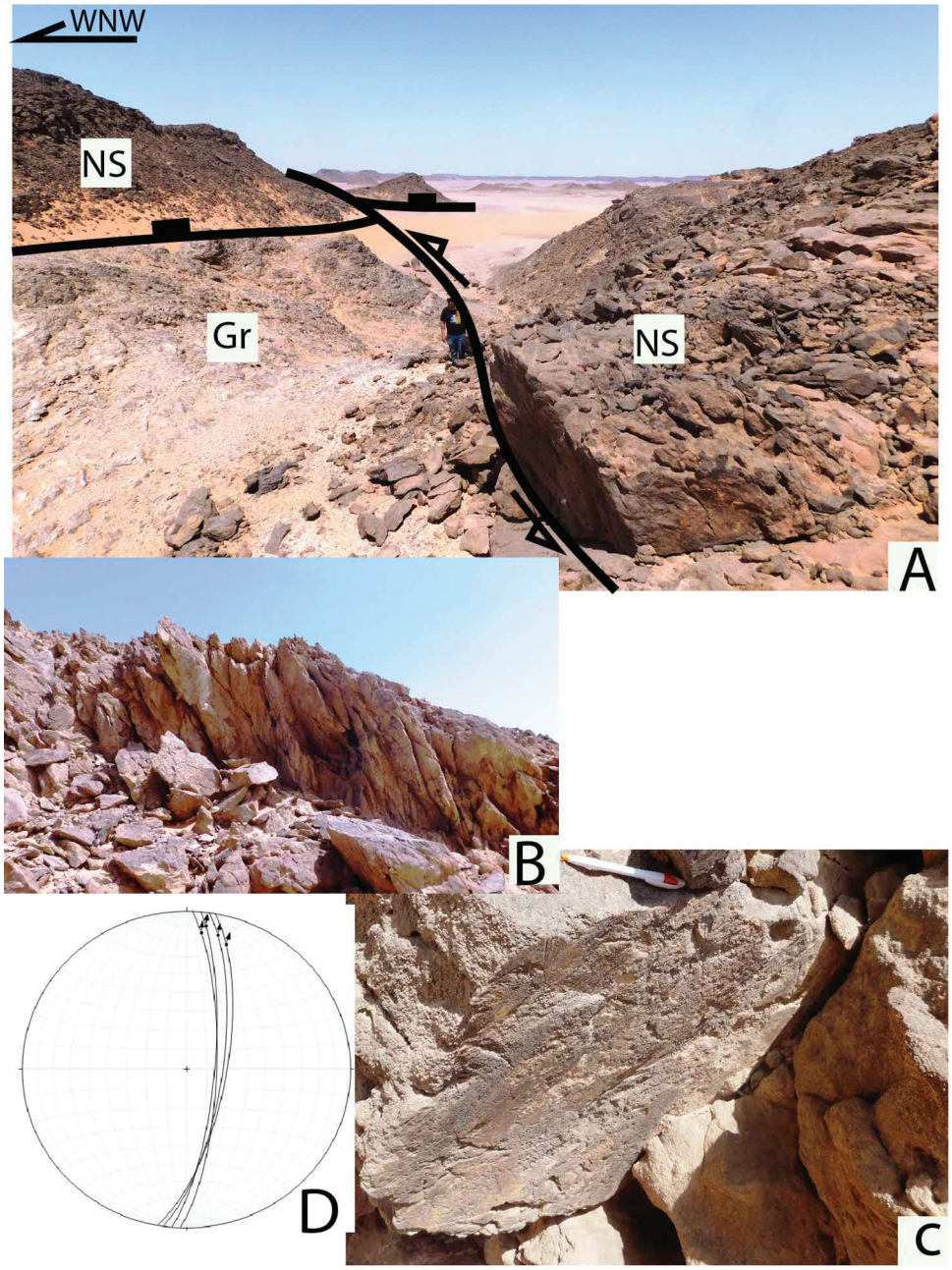

Figure 5. A: NNE-oriented fault intersects and sinistrally offset NW-oriented normal fault, B: high fracture intensity at the intersection zone, C: oblique slacklines on the NNE oriented fault, D: stereographic projection of the slip data of the NNE oriented fault.

Inherited WNW and NNE shear zones were reactivated as rift border and transfer fault during the Cretaceous extension. NNE faults are extended for ten kilometres and consist of several segments of the right-stepping array. NNE oriented faults are intersected and sinistrally offset NW oriented faults (Figure 5(A)). Zones of intersection are highly deformed and characterised by intensive fracture pattern (Figure 5(B)). Slickensides of the NNE faults are oblique, indicating strike-slip movement with minor dip-slip component (Figures 5C and D). Prolonged volcanic fields have been developed at the intersection between the WNW and NW rift border fault system and the NNE shear zone, e.g. Wadi Natash volcanic field (Figure 4). Wadi Natash volcanic field represents a basin extends for 50 km in length and 20 km in width. This basin system was filled by thick volcanic and volcanoclastic succession and bounded from the east by Precambrian basement rocks and from the west by Pre-rift Nubian sandstone

3.4. Recent seismic activities

Nubian Desert of Egypt witnessed recent seismic activities associated with neo-tectonics. Most seismic events were recorded along the NNE-oriented shear zone e.g. Terbiti and Timsah shear zone (Figure 6). Few seismic events have occurred along the E-W and NW oriented fault segments which intersected with the NNE fault. Morphometric evidence indicates right-lateral and left-lateral strike-slip movement

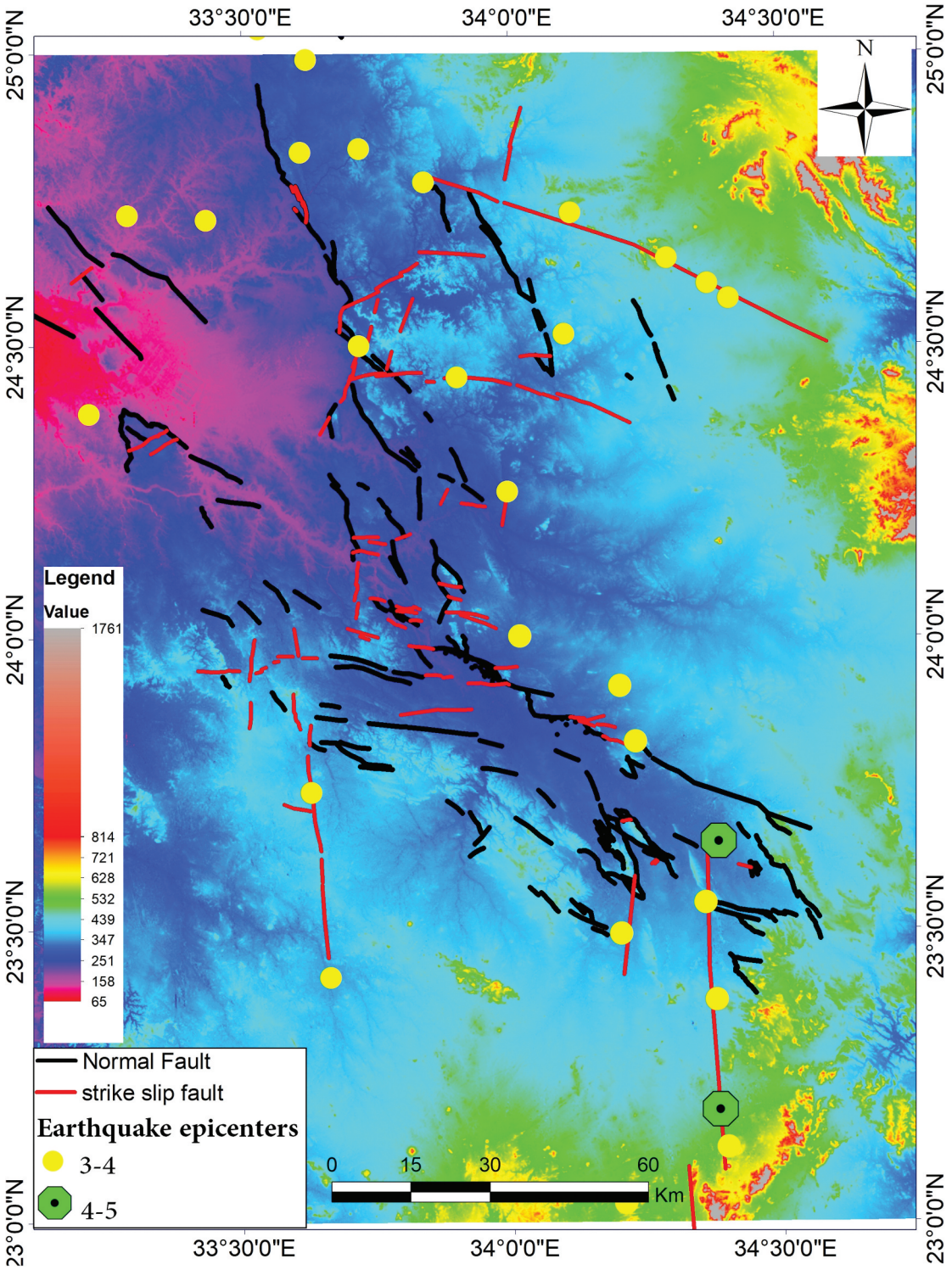

Figure 6. Distribution of earthquake epicentres epicentres and the fault pattern of the Nuqra-Natash and Garara regions.

along the E-W and NNE faults. Analysis of the area's major seismic events' focal mechanisms indicated WNW direction of SHmax and NE direction of SHmin (Fat-Helbary and Haggag 2004). The NNE sinistral fault system of the Eastern Desert of Egypt is considered the Red Sea's inland equivalent to transform faults. The seismic activity along NNE faults was associated with developing many co-seismic rupture surfaces with ENE, WNW, NNE, and E-W orientations. These seismic ruptures are localised at the intersection zones between the NNE and E-W oriented faults (Consultants., W.-C 1985; Sakran and Said 2018; Said 2019).

3.4.1. Structure control of nuqra-natash and garara rift system

Wadi Natash region has the highest LST value in the Nuqra-Kharit-Natash region. This zone is in the accommodation zone between two rift segments (Figure 5). Accommodation zones have more significant stretching than other rift portions and include numerous fault and fracture strands. Additionally, accommodation zones

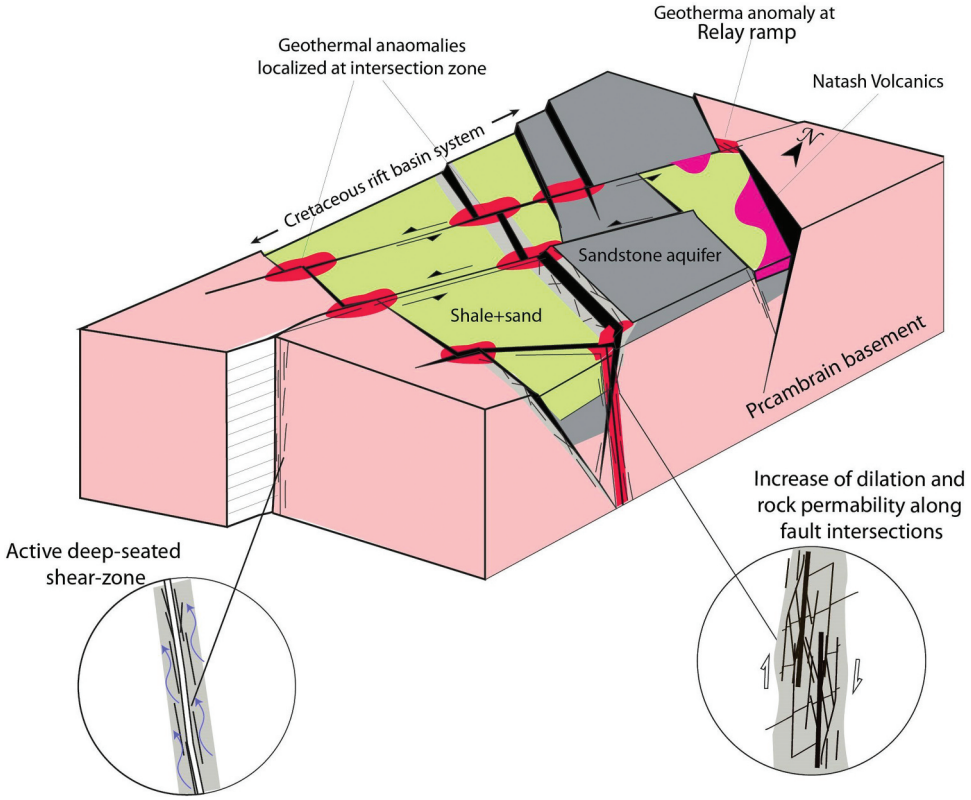

Figure 7. Block diagram shows the possible heat sources that produced the anomalous LST in Egypt.

exhibit stress localisation and reactivation and deep intersections of numerous faults to promote the deep circulation of fluids (Hinz et al. 2011).

The LST analysis wadi Natash thermal anomaly reveals the highest LST values observed at the Wadi Natash ring dyke's region, which developed at the intersection of the NW oriented Cretaceous rift system and active NE sinistral shear zone (Figure 3). LST values of Wadi Natash scored 52°C to 53°C along with NW and N-S oriented faults and 53°C – 54°C at the intersection of these two fault sets (Figure 7). Fault intersection zones are typically zones of intensive faulting and fracturing and much fluid movement (Micklethwaite and Cox 2004; Sheldon and Micklethwaite 2007; Hinz et al. 2011; Siler et al. 2016, 2018; Said 2022). Multiple overlapping fault strands and intersections between normal faults increase fracture density, enhance permeability, and concentrate geothermal fluids (McLachlan et al. 2011; Faulds et al. 2012; Said 2022). The investigation area witnessed seismic activity responsible for reactivating old trends, increasing fracture density, and enhancing permeability. Additionally, the developed co-seismic ruptures are localised to the intersection zone. All these criteria support the idea of the circulation of hydrothermal water at the intersection of N-S and NW oriented faults.

3.4.2. Regional comparison with Katwe geothermal site (East African rift valley), Uganda

Katwe Volcanic Field (KVF) lies on the western escarpment of the East African Rift. It is one of the three geothermal locations in Uganda that have had their geothermal potential examined. Recently, the government of Uganda inked a contract with an American business to build a 150-megawatt geothermal power plant in western Uganda, Kasese, and Katwe. A comparison of the Natash volcanic field, Egypt, with the Katwe Volcanic Field (KVF) revealed that 1) both are rift-related volcanic extruded at the shoulders of failed rift systems. The Precambrian basement rocks, Pleistocene-Pliocene volcanic, and Quaternary Lake sediments cover the KVF. It is dominated by pyroclastic material with lavas' rare occurrence and ejected lava blocks as accidental fragments. Wadi Natash volcanic field occurs at the eastern shoulder of Nuqra-Kharit basin. Volcanic-sedimentary rocks cover it and obey late Jurassic to Late Cretaceous times. 2) The geothermal surface manifestations in the Katwe volcanic field are hot springs, warm springs, and travertine deposits. The maximum surface temperature in the hot spring in Lake Kitagata Crater is 70°C, while Lake Katwe Crater is 32°C (Natukunda 2010). The geothermal surface manifestations observed at the Kom Ombo-Nuqra-Kharit rift basin's western shoulder include warm springs and travertine deposits (Nicoll

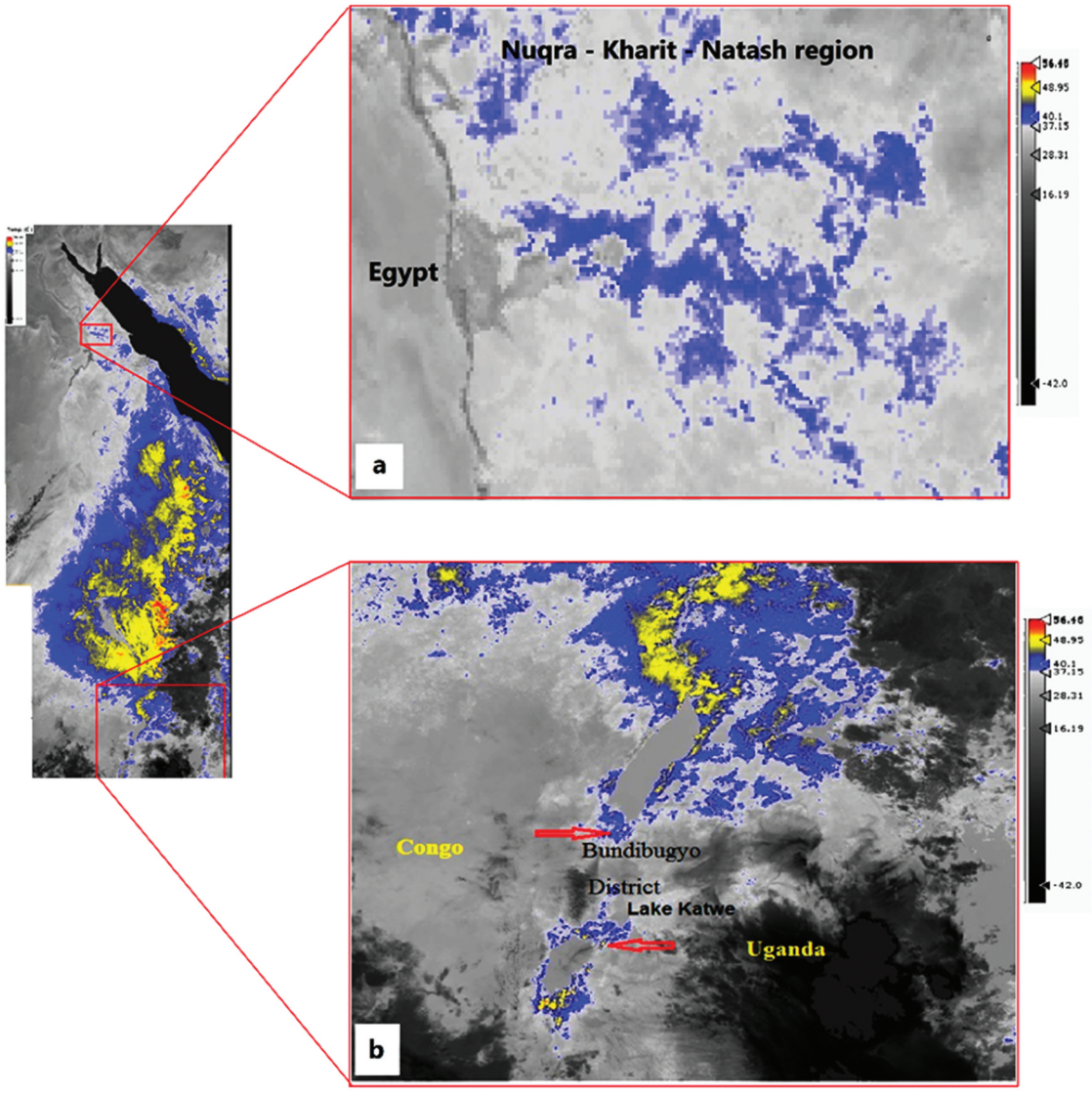

Figure 8. Sentinel-3 LST product acquired in March 2020 shows the East African region. a) LST subset for Natash volcanic field, Egypt. b) LST subset for Katwe volcanic region, Uganda.

and Sallam 2017). 3) Both areas have high geothermal gradients. The anomalous LST value of Katwe and Natash volcanic fields scored 58°C and 48°C, respectively, as measured from Sentinel-3 LST Product acquired in March 2020 (Figure 8).

4. Conclusions

The present study proved the Sentinel-3 LST products' usefulness to map the geothermal anomalies over the Egyptian territories. Seven LST thermal anomalies are retrieved from the Sentinel-3 LST products acquired in 2019 and confirmed using 2020 images. Three of them are recorded for the first time and attributed to the active sinistral strike-slip faults and the active shear zone's intersection with the intracontinental rift. These thermal anomalies are classified into two categories based on their possible heat sources. The first category represents a local heat source and is confined to the phosphate deposits. In contrast, the second category represents a deep heat source and controlled by an intersection pattern of rift-related faults and active N-S left-lateral strike-slip fault (Figure 7). The present study concluded that the Nuqra-Kharit-Natash region could be considered a promising geothermal site. Local LST anomalies in this region, hot springs and tufa deposits are strongly correlated with the active NNE-oriented fault zone and zones of intersection of this trend with the NW-oriented fault. These sites may be offered to the private sector interested in geothermal energy investment in Egypt. This work suggests that the LST analysis is an influential tool for detecting thermal anomalies at the regional scale, where it is fast, cost-effective, and highly efficient. Integration of remote sensing analysis with structural geology analysis impressively improves the applicability of LST as a tool for detection of the geothermal anomalies. The current approach is an exploration phase that aims to map the location of potential geothermal anomalies, which will be

studied in more detail by geophysical, drilling and in-depth geological models.

Acknowledgments

We are grateful to the editor and the reviewers for their effort to review our manuscript and for their valuable comments and discussions that improved our paper.

Disclosure statement

No potential conflict of interest was reported by the author(s).

ORCID

Said M. Said http://orcid.org/0000-0002-6274-9362

References

Abdelhalim A, Abuelella I, Sakran SM, Said SM. 2023. Implementation of space-borne optical data and field investigation for Geo-structural mapping of an interior Rift Basin: a case study from kharit area, Southeastern Desert, Egypt. J Min Environ. 14(4):1037–1059. doi: 10.22044/jme.2023.12739.2327.

Abdel Zaher M, El Nuby M, Ghamry E, Mansour K, Saadi NM, Atef H. 2014. Geothermal studies in oilfield districts of eastern margin of the Gulf of Suez, Egypt. NRIAG J Astron Geophysics. 3(1):62–69. doi: 10.1016/j.nrjag.2014.04.002.

Abdel Zaher M, El-Qady G, Elbarbary S. 2023. Geothermal potentiality of Egypt: review and updated status. 637–648. doi: 10.1007/978-3-030-95637-0_22.

Abdel Zaher M, Saibi H, Nouby ME, Ghamry E, Ehara S. 2011. A preliminary regional geothermal assessment of the Gulf of Suez, Egypt. J Afr Earth Sci. 60(3):117–132. doi: 10.1016/j.jafrearsci.2011.02.006.

Chan H-P, Chang C-P, Dao PD. 2018. Geothermal anomaly mapping using Landsat ETM+ data in Ilan Plain, Northeastern Taiwan. Pure Appl Geophys. 175 (1):303–323. doi: 10.1007/s00024-017-1690-z.

Chorowicz J. 2005. The East African rift system. J Afr Earth Sci. 43(1–3):379–410. doi: 10.1016/j.jafrearsci.2005.07.019.

Coll C, Caselles V. 1997. A split-window algorithm for land surface temperature from advanced very high resolution radiometer data: validation and algorithm comparison. J Geophys Res. 102(D14):16697–16713. doi: 10.1029/97JD00929.

Consultants. W.-C. 1985. Seismic geology and tectonics studies of the Aswan region. In: Earthquake activity and dam stability evaluations for the Aswan high dam, Egypt for the high and Aswan dams authority, ministry of irrigation, Arab Republic of Egypt. Internal report; p. 3.

Coolbaugh MF, Kratt C, Fallacaro A, Calvin WM, Taranik JV. 2007. Detection of geothermal anomalies using advanced spaceborne thermal emission and reflection radiometer (ASTER) thermal infrared images at Bradys Hot Springs, Nevada, USA. Remote Sens Environ. 106(3):350–359. doi: 10.1016/j.rse.2006.09.001.

Darge YM, Hailu BT, Muluneh AA, Kidane T. 2019. Detection of geothermal anomalies using Landsat 8 TIRS data in Tulu Moye geothermal prospect, Main Ethiopian Rift. Int J Appl Earth Obs Geoinf. 74:16–26.

DiPippo R. 2005. Geothermal power plants: principle, applications and case studies. 1st ed. (UK): Elsevier.

Elbarbary S, Abdel Zaher M, Mesbah H, El-Shahat A, Embaby A. 2018. Curie point depth, heat flow and geothermal gradient maps of Egypt deduced from aeromagnetic data. Renewable Sustain Energy Rev. 91:620–629. doi: 10.1016/j.rser.2018.04.071.

El-Qady G. 2006. Exploration of a geothermal reservoir using geoelectrical resistivity inversion: case study at Hammam Mousa, sinai, Egypt. J Geophys Eng. 3 (2):114–121. doi: 10.1088/1742-2132/3/2/002.

El-Sayed S, H. M ; and Ibrahim. 2006. Mar. Chemical and geothermal studies on the groundwater of dakhla oasis, Western Desert, Egypt. 1–26. https://www.researchgate.net/publication/270957028.

Fat-Helbary R, Haggag M. 2004. Seismicity and seismotectonics of the West Kom Ombo Area, Aswan, Egypt. Acta Geodyn Geomater. 1(2 (134)):195–200.

Faulds JE, Hinz N, Kreemer C, Coolbaugh M. 2012. Regional patterns of geothermal activity in the Great Basin Region, Western USA: correlation with strain rates. Geotherm Resour Counc Transaction. 36:897–902.

Gad E-Q, Ushijima K, Ahmed E. 2000. Delineation of Geothermal Reservoir by 2D inversion of resistivity data at hamam faraun area, sinai, Egypt. World Geotherm Congr. 2000:1103–1108.

Gad MI. 2011. Optimal management for groundwater of Nubian aquifer in El Dakhla depression, Western Desert, Egypt. Int J Water Res Environ Eng. 3(14). doi: 10.5897/IJWREE11.103.

GEO. 2018. 13th Middle East Geosciences Conference and Exhibition; Manama, Bahrain.

Haselwimmer C, Prakash A, Holdmann G. 2011. Geothermal exploration at Pilgrim Hot Springs, Alaska using airborne thermal infrared remote sensing. Trans - Geotherm Resour Counc. 35(1):805–810.

Hinz N, Faulds J, Stroup C. 2011. Stratigraphic and structural framework of the Reese River Geothermal Area, Lander County, Nevada: a new conceptual structural model. Geotherm Resour Counc Trans. 35:827–832.

Jimenez-Munoz JC, Sobrino JA, Skokovic D, Mattar C, Cristobal J. 2014. Land surface temperature retrieval methods from Landsat-8 thermal infrared sensor data. IEEE Geosci Remote Sens Lett. 11(10):1840–1843. doi: 10.1109/LGRS.2014.2312032.

King D, Metcalfe E. 2013. Rift zones as a case study for advancing geothermal occurrence models. *PROCEEDINGS: Thirty-Eighth Workshop on Geothermal Reservoir Engineering*, February 11-13, 2013, Stanford University, Stanford, California. p. 11.

Lashin A. 2007. Evaluation of the geothermal potential around the coastal parts of the Gulf of Suez, Egypt, using well logging and the geothermometer data. Applied Geophgys. 6(2):215–248.

Lashin A. 2013. A preliminary study on the potential of the geothermal resources around the Gulf of Suez, Egypt. Arab J Geosci. 6(8):2807–2828. doi: 10.1007/s12517-012-0543-4.

Lashin A. 2015. Geothermal resources of Egypt: country update. *Proceedings World Geothermal Congress* p. 19–25. (April).https://pangea.stanford.edu/ERE/db/WGC/papers/WGC/2015/01073.pdf.

Lashin A, Al Arifi N. 2010. Some aspects of the geothermal potential of Egypt case study: gulf of suez-Egypt. *Proceedings World Geothermal Congress* p. 25–29. (April).https://s3.amazonaws.com/academia.edu.documents/3464287/1196.pdf?AWSAccessKeyId=AKIAIWO

WYYGZ2Y53UL3A&Expires=1535559785&Signature=9PxVdsnS7ZqKCXVDBjsa8J5wC7o%3D&response-content-disposition=inline%3B filename%3DSome_Aspects_of_Geothermal_Potential_of.pdf.

Lee K. 1978. Analysis of thermal infrared imagery of the Black Rock Desert geothermal area. Geology. 73(3):3–43.

Madani AA. 2012. Discrimination of jurassic volcanicity in strike-slip basin, Jabal Al Maqtal area, South Eastern Desert, Egypt, using ASTER and field data. J King Abdulaziz Univ Earth Sci. 23(2): 1–18. doi: 10.4197/Ear.23-2.1.

Madani AA. 2020. Mapping geothermal anomalies in Rift-Related Wadi Natash Volcanic Field, South Eastern Desert, Egypt using thermal infrared and SAR remote sensing techniques. *13th International Geological Conference*; Jeddah, Saudi Arabia.(Abstract). 03-05 March 2020,

McLachlan H, Benoit W, Faulds J. 2011. Structural framework of the Soda Lake Geothermal Area, Churchill County, Nevada. Geotherm Resour Counc Trans. 35:925–930.

Micklethwaite S, Cox SF. 2004. Fault-segment rupture, aftershock-zone fluid flow, and mineralization. Geology. 32(9):813. doi: 10.1130/G20559.1.

Morgan P, Swanberg CA. 1978. Heat flow and the geothermal potential of Egypt. Pure Appl Geophysics PAGEOPH. 117(1–2):213–226. doi: 10.1007/BF00879748.

Moustafa A, Sehim A, Farouk O. 2016. Hydrocarbon assessments of interior cretaceous rift basins, Upper Egypt. *13th Mediterranean Offshore Conference and Exhibition in Alexandria, Egypt*, Alexandria. p. 1–14.

Natukunda JF. 2010. Geology of Kibiro, Katwe and buranga geothermal prospects of Uganda. *Proceedings World Congress 2010*; Bali, Indonesia; 25–29. (April).

Nicoll K, Sallam ES. 2017. Paleospring tufa deposition in the Kurkur Oasis region and implications for tributary integration with the River Nile in southern Egypt. J Afr Earth Sci. 136(November 2016):239–251. doi: 10.1016/j.jafrearsci.2016.10.014.

Qin Q, Zhang N, Nan P, Chai L. 2011. Geothermal area detection using Landsat ETM+ thermal infrared data and its mechanistic analysis—A case study in Tengchong, China. Int J Appl Earth Observ Geoinf. 13(4):552–559. doi: 10.1016/j.jag.2011.02.005.

Sadek M. 1996. Hydrogeological and environmental isotopes studies on the Nubian aquifer in scattered regions at the Western Desert, Egypt. Egypt: Ain Shams University.

Said SM. 2019. Structure setting and tectonic evolution of the southeastern part of the Western Desert of Egypt. PhD thesis, Cairo University.

Said SM. 2022. Fault control and timing of manganese deposits at Abu Ramad, South Egyptian margin of the Red Sea. Int Geol Rev. 65(14):2256–2268. doi: 10.1080/00206814.2022.2137703.

Said SM, Sakran S. 2020. Structural analysis and tectonic evolution of the Komombo basin, south Egypt; an example of interior cretaceous rift. J Afr Earth Sci. 162:103719. doi: 10.1016/j.jafrearsci.2019.103719.

Said SM, Sakran S. 2022. Geometry and kinematics of right□lateral transpressional faults and growth folds, the western side of the Gulf of Suez, Egypt. Geological J. 57(1):276–291.

Sakran S, Said SM. 2018. Structural setting and kinematics of Nubian fault system, SE Western Desert, Egypt: an example of multi-reactivated intraplate strike-slip faults. J Struct Geol. 107:93–108. doi: 10.1016/J.JSG.2017.12.006.

Sehim A. 1993. Cretaceous tectonic in Egypt. Egypt J Geol. 37–1:335–372.

Sekertekin A, Arslan N. 2019. Monitoring thermal anomaly and radiative heat flux using thermal infrared satellite imagery – a case study at Tuzla geothermal region. Geothermics. 78:243–254. doi: 10.1016/j.geothermics.2018.12.014.

Sheldon HA, Micklethwaite S. 2007. Damage and permeability around faults: implications for mineralization. Geology. 35(10):903–906. doi: 10.1130/G23860A.1.

Siler DL, Hinz NH, Faulds JE. 2018. Stress concentrations at structural discontinuities in active fault zones in the western United States: implications for permeability and fluid flow in geothermal fields. GSA Bull. 130(7–8):1273–1288. doi: 10.1130/B31729.1.

Siler DL, Hinz NH, Faulds JE, Queen J. 2016. 3D analysis of geothermal fluid flow favorability: Brady's, Nevada, USA. In Proceedings, forty-first workshop on geothermal reservoir engineering. Stanford: Stanford University.

Sobrino JA, Raissouni N. 2000. Toward remote sensing methods for land cover dynamic monitoring: application to Morocco. Int J Remote Sens. 21(2):353–366. doi: 10.1080/014311600210876.

Srivastava PK, Majumdar TJ, Bhattacharya AK. 2009. Surface temperature estimation in Singhbhum Shear Zone of India using Landsat-7 ETM+ thermal infrared data. Adv Space Res. 43(10):1563–1574. doi: 10.1016/j.asr.2009.01.023.

Taha MA, Aziz H. 1998. Mesozoic rifting in Upper Egypt concession (abs). 14th International Petroleum Conference; Cairo, Egypt. p. 5.

Tolba M. 2014. An analytical study of the architecture and imran environmentally sensitive areas (the case of the Springs of hot water oases). Int J Curr Eng Technol. 4(2):919–928.

van der Meer F, Hecker C, van Ruitenbeek F, van der Werff H, de Wijkerslooth C, Wechsler C. 2014. Geologic remote sensing for geothermal exploration: a review. Int J Appl Earth Observ Geoinf. 33:255–269. doi: 10.1016/j.jag.2014.05.007.

Wysick P. 1987. Contribution to the subsurface geology of the misaha trough and the southern Dakhla basin (S. EgyptLN. Sudan). Berl Geowiss. 75((A)(1)):137–150.

Zaher MA, Elbarbary S. 2021. Investigation of geothermal resources in Egypt using geophysical data. Proceedings World Geothermal Congress; Reykjavik, Iceland, p. 1–4.

Zaher MA, Saibi H, Nishijima J, Fujimitsu Y, Mesbah H, Ehara S. 2012. Exploration and assessment of the geothermal resources in the Hammam Faraun hot spring, Sinai Peninsula, Egypt. J Asian Earth Sci. 45:256–267. doi: 10.1016/j.jseaes.2011.11.007.

Zaher M, Ehara S. 2009. Heat flow and geothermal resources in Egypt. J Geotherm Res Soc Jpn. 31(3):155–166. doi: 10.11367/grsj.31.155.

Zheng Y, Ren H, Guo J, Ghent D, Tansey K, Hu X, Nie J, Chen S. 2019. Land surface temperature retrieval from sentinel-3A sea and land surface temperature radiometer, using a Split-window algorithm. Remote Sens. 11(6):650. doi: 10.3390/rs11060650.